

The Most Sensitive Initial Error of Sea Surface Height Anomaly Forecasts and Its Implication for Target Observations of Mesoscale Eddies

LIN JIANG,^{a,b} WANSUO DUAN,^{a,b} AND HAILONG LIU^{a,b}

^a *LASG, Institute of Atmospheric Physics, Chinese Academy of Sciences, Beijing, China*

^b *University of Chinese Academy of Sciences, Beijing, China*

(Manuscript received 8 September 2021, in final form 5 January 2022)

ABSTRACT: We used the conditional nonlinear optimal perturbation (CNOP) approach to investigate the most sensitive initial error of sea surface height anomaly (SSHA) forecasts by using a two-layer quasigeostrophic model and revealed the importance of mesoscale eddies in initialization of the SSHA forecasts. Then, the CNOP-type initial errors for individual mesoscale eddies were calculated, revealing that the errors tend to occur in locations where the eddies present a clear high-to-low-velocity gradient along the eddy rotation and the errors often have a shear SSHA structure present. Physically, we interpreted the rationality of the particular location and shear structure of the CNOP-type errors by barotropic instability from the perspective of the Lagrange expression of fluid motions. Numerically, we examined the sensitivity of the CNOP-type errors by using observing system simulation experiments (OSSEs). We concluded that if additional observations are preferentially implemented in the location where CNOP-type errors occur, especially with a particular array indicated by their shear structure, the forecast ability of the SSHA can be significantly improved. These results provide scientific guidance for the target observation of mesoscale eddies and therefore are very instructive for improving ocean state SSHA forecasts.

KEYWORDS: Eddies; Optimization; Forecasting; Uncertainty

1. Introduction

Ocean mesoscale eddies are known as coherent rotating vortices of water, with radii ranging from tens to hundreds of kilometers and lifespans ranging from dozens to hundreds of days (Chelton et al. 2007; Faghmous et al. 2015). They occupy approximately 25% of the global ocean surface area at any given time and are a ubiquitous feature of ocean basins (Gaube et al. 2014). Mesoscale eddies are strongly constrained by Earth's rotation and ocean stratification, such that their motions can be an approximation to the geostrophic balance (Zhang et al. 2013). Mesoscale eddies are energetically dominant and significantly influence oceanic dynamics and ocean mixing, having the ability to transport momentum, heat, salt, and biogeochemical tracers along their trajectories (Villas Bôas et al. 2015). Mesoscale eddies play a critical role in the dynamics of major oceanic current systems, such as the Antarctic Circumpolar Current, the Kuroshio, and the Gulf Stream (Hallberg 2013). They have also been shown to influence the overlying atmosphere, such as winds, clouds, precipitation, and typhoons, etc. (Chelton 2013). Thus, knowledge of mesoscale eddies and their motions has important implications for depicting future ocean states and associated biological, chemical, and geological oceanography (Robinson 1983), as well as depicting future atmospheric conditions (Frenger et al. 2013).

Ocean circulation can be regarded as a turbulent system full of vortices (Morrow and Le Traon 2012). Babiano et al. (1994) demonstrated that such a vortex-dominated turbulence system is significantly controlled by the chaotic motion of the

vortices. From this perspective, Weiss and Grooms (2017) showed that accurate initialization of mesoscale eddies leads to improved estimates and forecasts of the future sea surface height (SSH) by using a two-layer quasigeostrophic model. In particular, they found that assimilating a subset of observations on regular and equally spaced grids covering the entirety of the model scope is less effective than assimilating observations taken over mesoscale eddies. In their work, the assimilation strategy of mesoscale eddies was to assimilate observations on evenly distributed regular grids over eddies. However, mesoscale eddies are irregular in shape and asymmetric in the flow field, which reduces the stability of the vortex structure and enhances the energy conversion, which presents a highly nonlinear nature (Tang et al. 2020). Therefore, there may be a much more effective assimilating strategy for the initialization of irregular eddies than that suggested by Weiss and Grooms (2017). Inferentially, there should exist an area over the mesoscale eddies, where evenly distributed regular grid observations should be preferentially rearranged to adapt to irregular eddies and then assimilated to achieve a much larger improvement in the SSH forecasting ability. Addressing this problem can also inform us of which area should be given priority to implement additional observations for mesoscale eddies associated with the SSH forecasts. Such questions are generally related to an observational strategy entitled "target observation" (Snyder 1996).

The target observation mainly serves the demand of forecasts on observations (Snyder 1996), which is different from traditional observation strategies, that is, to recognize the phenomenon and understand its mechanism. The so-called target observation strategy was developed in the 1990s. The idea is described as follows: to better predict an event at a future time t_2 (i.e., verification time) in a focused area (i.e.,

Corresponding author: Wansuo Duan, duanws@lasg.iap.ac.cn

DOI: 10.1175/JPO-D-21-0200.1

© 2022 American Meteorological Society. For information regarding reuse of this content and general copyright information, consult the [AMS Copyright Policy](#) (www.ametsoc.org/PUBSReuseLicenses).

Brought to you by Institute of Atmospheric Physics, CAS | Unauthenticated | Downloaded 04/08/22 12:44 AM UTC

verification area), additional observations are deployed at a future time t_1 (i.e., target time; $t_1 < t_2$) in some key areas (i.e., sensitive areas) where additional observations are expected to have a large contribution to reducing the prediction errors in the verification area (Snyder 1996; Mu et al. 2015). These additional observations are incorporated by a data assimilation system to form a more reliable initial state, which would be supplied to the model for a more accurate prediction (Mu et al. 2015). A series of encouraging results have been achieved in theoretical research and related field experiments of target observations for high-impact weather and climate event forecasting. In particular, The Observing Systems Research and Predictability Experiment (THORPEX), a global atmospheric research program organized by the World Meteorological Organization from 2005 to 2014, used the target observation strategy to reveal the important role of the additional observations in sensitive areas in improving the forecasting ability of typhoon tracks. Since 2003, the program of Dropwindsonde Observation for Typhoon Surveillance near the Taiwan Region (DOTSTAR), one of its most critical objectives just is target observations, has been conducted under the support of the National Science Council (NSC) in Taiwan and has obtained many valuable data for operational forecasting (Wu et al. 2007, 2009). However, THORPEX and DOTSTAR mainly adopted methods of linear approximation to determine the sensitive area of target observations, which is not allowed to adequately investigate the nonlinear evolution of the initial errors and may cause the resulting sensitive area to deviate from the real one of high-impact weather and climate event forecasts, thus suppressing the operational effect of the target observations (Yu et al. 2017). To fully take nonlinearity into account, Mu et al. (2003) proposed a nonlinear technique of target observation, i.e., the approach of conditional nonlinear optimal perturbation (CNOP; see also Mu et al. 2003, 2009). The so-called CNOP represents the initial perturbation that belongs to a certain physical constraint and causes the largest perturbation growth at a determined future time and acts as the most sensitive initial perturbation in a nonlinear model, therefore having potential for identifying sensitive areas for targeting observations (Mu et al. 2009). Practically, the CNOP has been applied to the studies of targeting observations associated with El Niño–Southern Oscillation (ENSO), the Indian Ocean dipole (IOD), tropical cyclones (TCs), and the Kuroshio large meander (KLM) (Duan et al. 2018; Mu et al. 2017; Qin et al. 2013; Li et al. 2014; Wang et al. 2013) and identified their respective optimal locations for targeting observations (Mu et al. 2015).

As reviewed above, the initialization of oceanic mesoscale eddies can determine the accuracy of future ocean state forecasts. Furthermore, it is known that targeted observations play a critical role in improving the initialization of numerical forecasts. For mesoscale eddies, satellite observations of the SSH/SSHA can be obtained to depict mesoscale eddies; however, they still cause considerable uncertainty in the real-time forecasts, which requires a higher time sampling rate of observations (Cotton and Menard 2006). In

particular, observations for disclosing the subsurface structures of eddies are still avoided, which is very important for exploring eddy dynamics and evaluating eddy-induced water mass transport (Roemmich and Gilson 2001). In this scenario, field observations are a useful complement (Zhang et al. 2019). However, field observations of mesoscale eddies are very expensive, especially for mesoscale eddies in regions far away from continents (Dickey et al. 2008; Zhang et al. 2019). Therefore, we suggest that one should consider using the economic target observation strategy to obtain a limited number of the most effective additional observations for improving the initialization of mesoscale eddies. In fact, even if satellite observations and field observations are sufficient, one should also consider which observations should be preferentially assimilated to the model initial fields to achieve much higher forecasting skill of relevant ocean states, as doing in Weiss and Grooms (2017). Therefore, in any case, we should identify the sensitive areas for target observations, where observations should be preferentially assimilated to the model initial field to improve the forecasting ability of the concerned state variables.

In the present study, we investigated the optimal locations (i.e., sensitive area) for target observations of mesoscale eddies, and to facilitate a comparison, a two-equal-layer quasigeostrophic (QG) model (Grooms and Majda 2014), similarly to that in Weiss and Grooms (2017), was adopted except that this model is a perturbation model of potential vorticity and then the forecasts here are made for the ocean state sea surface height anomaly (SSHA). The CNOP, due to it fully considering nonlinear effects, has shown great potential in identifying the optimal locations for targeting observations associated with high-impact weather and climate event forecasts. Thus, considering the highly nonlinear nature of mesoscale eddies, we can reasonably adopt the CNOP approach for identifying the sensitive area of the SSHA forecasts.

The rest of the article is organized as follows. The two-layer quasigeostrophic model is introduced in section 2, and the CNOP approach is briefly reviewed in section 3. Section 4 explores the CNOPs of the SSHA forecasts and reveals the importance of the initialization of mesoscale eddies in improving the SSHA forecasts. In section 5, sensitivity to the CNOP superimposed on initial eddies are examined, and in section 6 observing system simulation experiments are conducted to confirm the rationality of the sensitive area for target observations identified by CNOP associated with SSHA forecasts. Finally, a summary and discussion are presented in section 7.

2. The two-layer quasigeostrophic model

The two-equal-layer quasigeostrophic (QG) model is established on an f plane, which describes a doubly periodic flow with a rigid lid boundary and is forced by an imposed, baroclinically unstable, horizontally uniform and vertically sheared zonal flow. An instantaneous flow field can be decomposed into a mean field and a perturbation field. With this decomposition of the flow field, the nondimensional governing

equations of the perturbation evolution derived by the two-layer QG model can be written as follows:

$$\partial_t q_1 = -\mathbf{U}_1 \cdot \nabla q_1 - \partial_x q_1 - v_1 - \nu \nabla^8 q_1, \tag{1}$$

$$\begin{aligned} \partial_t q_2 = & -\mathbf{U}_2 \cdot \nabla q_2 + \partial_x q_2 + v_2 \\ & -c_d \cdot \nabla \times (|\mathbf{U}_2| \mathbf{U}_2) - \nu \nabla^8 q_2, \end{aligned} \tag{2}$$

$$q_1 = \nabla^2 \psi_1 + \frac{1}{2}(\psi_2 - \psi_1), \tag{3}$$

$$q_2 = \nabla^2 \psi_2 - \frac{1}{2}(\psi_2 - \psi_1), \tag{4}$$

where q_i and ψ_i ($i=1, 2$ represent the upper and lower layers) denote the potential vorticity and streamfunction, $u_i = -\partial_y \psi_i$, $v_i = -\partial_x \psi_i$ are the zonal and meridional velocities and constitute the two-dimensional vector \mathbf{U}_i , and c_d ($=0.1$) and ν ($=5 \times 10^{-7}$) denote the standard quadratic drag coefficient and hyperviscosity coefficient, respectively. The model configuration follows that used in Weiss and Grooms (2017). The equations, as mentioned above, are nondimensional, where the imposed zonal velocity and the deformation radius are adopted as the velocity scale and length scale, respectively. Specifically, the model domain is a square and has a nondimensional width 32π ; the nondimensional grid size is 0.39, which can include more than two grid points per deformation radius and is sufficient for eddy-resolving computations of this kind; with a nondimensional time step of 0.01. According to Weiss and Grooms (2017), a dimensional value of 15 km was assigned to the spatial grid size and a dimensional value of 0.01 m s^{-1} to the velocity; thus, the dimensional deformation radius was 38.2 km, the dimensional domain width was 3840 km, and the dimensional time scale was approximately 42 days (i.e., 6 weeks). The numerical solutions of the model were computed using 256×256 nonzero Fourier modes and a fourth-order semi-implicit Runge–Kutta scheme.

3. Conditional nonlinear optimal perturbation

The CNOP describes the initial perturbation that satisfies a certain physical constraint and has the largest nonlinear evolution at a given prediction time (Mu et al. 2003). Similar optimal perturbation approaches were also subsequently suggested in the fields of fluid mechanics (see Pringle and Kerswell 2010; Kerswell et al. 2014). They are often formulated as follows.

Assume that the model governing the motions of the fluid is defined as follows:

$$\begin{cases} \frac{\partial \mathbf{U}}{\partial t} + F(\mathbf{U}) = 0 \\ \mathbf{U}|_{t=0} = \mathbf{U}_0, \end{cases} \tag{5}$$

where t is the time, F is a nonlinear partial differential operator, \mathbf{U} is the state vector, and \mathbf{U}_0 is its initial state. With different initial states of \mathbf{U}_0 and $\mathbf{U}_0 + \mathbf{u}_0$, they evolve into \mathbf{U}_T and $\mathbf{U}_T + \mathbf{u}_T$ at the prediction time T in Eq. (5). Then, we have Eq. (6) as follows:

$$\mathbf{U}_T = M_T(\mathbf{U}_0), \quad \mathbf{U}_T + \mathbf{u}_T = M_T(\mathbf{U}_0 + \mathbf{u}_0), \tag{6}$$

where M_T is a nonlinear propagator that takes an initial value to the prediction time T , so \mathbf{u}_T describes the evolution of the initial perturbation \mathbf{u}_0 of the reference state \mathbf{U}_T (\mathbf{U}_0 is its initial value).

The initial perturbation $\mathbf{u}_{0\delta}$ is called a CNOP if and only if

$$J(\mathbf{u}_{0\delta}) = \max_{\mathbf{u}_0 \in C_\delta} J(\mathbf{u}_0), \tag{7}$$

where $J(\mathbf{u}_0) = \|M_T(\mathbf{U}_0 + \mathbf{u}_0) - M_T(\mathbf{U}_0)\|$ is the cost function that evaluates the nonlinear evolution of the initial perturbation \mathbf{u}_0 at time T in terms of a norm and C_δ constrains the scope of the initial perturbations. Mathematically, CNOP is the global maximum of $J(\mathbf{u}_0)$ over the constraint C_δ . A specific CNOP does not depend on \mathbf{u}_0 in C_δ ; however, it could change for different prediction times T . For a constraint condition defined by a L2 norm, CNOP has been theoretically proved to locate on the boundary of the domain of the constraint condition. For more details, readers are referred to Duan and Mu (2009) for a review of CNOP.

In predictability studies, the CNOP represents the initial error that causes the largest prediction error at prediction time (Mu et al. 2003; Duan and Mu 2009). Therefore, for a prediction system, if one computes the CNOP-type errors of the predictions for historical states represented by a set of observations and estimates the prediction errors caused by them and if these prediction errors are still smaller than allowable prediction error, then the predictions to the future states made by this prediction system are most likely to be reliable and confident (Duan and Mu 2009). That is to say, the CNOP approach can be in this way to estimate a confidence level in predictions. In addition, the CNOP can also be used to yield initial perturbations in ensemble forecast and estimate the prediction uncertainties, then evaluating the confidence level of predictions (Duan and Huo 2016). The present study would use the CNOP approach to identify the sensitive area for target observation associated with SSHA forecasts and indicate the importance of meso-scale eddy initialization by using the two-layer QG model in section 2.

For the two-layer QG model, the SSHA was forecasted, and the CNOPs of the initial SSHA was calculated, where the SSHA was represented by the ψ_1 (i.e., the streamfunction in the upper layer; see section 2). Therefore, the cost function in Eq. (7) was expressed as $J(\psi_{1,0}^p) = \|M_T(\psi_{1,0} + \psi_{1,0}^p) - M_T(\psi_{1,0})\|$, where $\psi_{1,0}$ is the initial state of ψ_1 (which is referred to as a reference state to be predicted), $\psi_{1,0}^p$ is its initial perturbation and $\|\cdot\|$ is a L2 norm measuring the distance between reference state and its perturbation at the future time T .

Equation (8), i.e., the C_δ in Eq. (7), was used to constrain the amplitude of initial perturbations, which describes the root-mean-square of initial perturbations on grid points normalized by the standard deviation of initial SSHA and is described as follows:

$$C_\delta = \left\{ \psi_{1,0}^p \left| \sqrt{\frac{1}{n} \sum_{i=1}^n (\psi_{1,0}^p)_i^2} \leq \beta (\psi_{1,0})_{\text{STD}} \right. \right\}, \quad (8)$$

where n is the number of grid points perturbed, $(\psi_{1,0})_{\text{STD}}$ is the standard deviation of the $\psi_{1,0}$ on the grid points over the whole model scope and β is a preassigned positive number that was used to constrain the largest magnitude of the initial perturbations. Then the CNOP of the SSHA forecasts can be solved by Eq. (9):

$$J(\psi_{0\delta}^p) = \max_{\psi_{1,0}^p \in C_\delta} J(\psi_{1,0}^p), \quad (9)$$

where it accords to the practical observational errors of the SSHA and takes $\beta = 0.04$, which guarantees that the initial perturbations of SSHA do not exceed the dimensional observational errors of 0.02–0.03 m at each grid point. In addition, since the SSHA observations obtained from a flock of satellites were generally processed into weekly grid SSHA data products and then a 7-day assimilation window has been used to the initialization of the SSHA forecasting (see Weiss and Grooms 2017), we used 7 days as the optimization time interval of calculating the CNOP and identifying the sensitive areas for targeting observations of mesoscale eddies associated with the SSHA forecasting with lead time 7 days. Equation (8) indicates that initial perturbations belong to a physical constraint defined by L2 norm. Then Eq. (9) together with Eq. (8) guarantee the existence of CNOP; furthermore, they ensure that the CNOP locates on the boundary of the constraint condition Eq. (8) (see Duan and Mu 2009).

A key step to applying the CNOP approach was determining how to obtain the CNOP numerically by Eq. (9) because it is almost impossible to obtain an analytical solution to such a nonlinear optimization problem of high dimensions. In recent years, different algorithms, such as spectral projected gradient 2 (SPG2) (Birgin et al. 2000), sequential quadratic programming (SQP) (Barclay et al. 1997), and limited-memory Broyden–Fletcher–Goldfarb–Shanno (L-BFGS) (Liu and Nocedal 1989), have been adopted to obtain the CNOP according to different physical problems of concern. In the present study, the SPG2 algorithm was chosen to calculate the CNOP. It is noted that the SPG2 algorithm were generally designed to solve a minimum problem of nonlinear function within an initial constraint condition, where the gradient of the cost function with respect to initial perturbations was needed to represent the descending direction of searching for the minimum of the cost function. Therefore, for the problem of concerns here, we had to rewrite Eq. (9) as $J(\psi_{0\delta}^p) = \min_{\psi_{1,0}^p \in C_\delta} [-J(\psi_{1,0}^p)]$. Specifically, a first guess is assigned to the initial perturbation $\psi_{1,0}^p$. Then the QG model is integrated forward with the initial value of $\psi_{1,0} + \psi_{1,0}^p$ to obtain the forecast $M_T(\psi_{1,0} + \psi_{1,0}^p)$ with the reference state $M_T(\psi_{1,0})$ and the negative of the cost function, $-J(\psi_{1,0}^p)$, can be obtained. Then the gradient of the negative of the cost function with respect to the initial perturbations is calculated. Expectantly, the gradient here represents the fastest des-

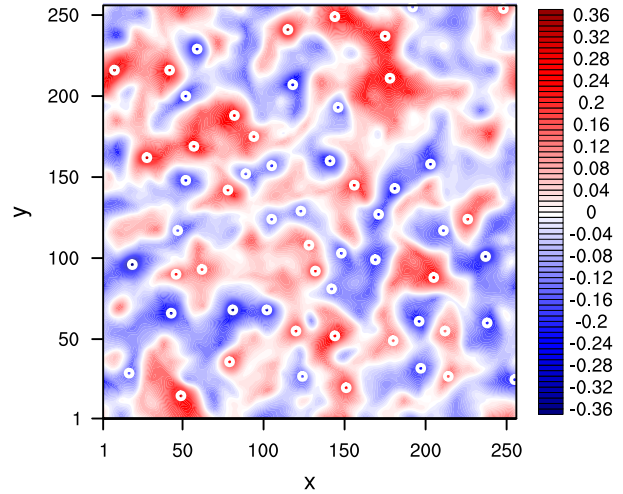


FIG. 1. The SSHA field (m) ψ_1 and associated mesoscale eddies generated by the two-layer QG model when it is integrated to the time T_0 with the initial value represented by a matrix comprised of random numbers satisfying the normal distribution $N(0, 1)$ of ψ . The white circles represent the centers of mesoscale eddies with blue cyclonic and red anticyclonic eddies.

cending direction of the cost function. However, in numerical experiments, CNOP can be obtained as long as the gradient keeps a fast descending direction but does not necessarily belong to the fastest. But in this situation, there will need much more time costs of the SPG2. Based on the automatically and iteratively forward integration of the two-layer QG model governed by the SPG2, the initial perturbation $\psi_{1,0}^p$ is optimized and updated according to the gradient till the convergence condition in the SPG2 is satisfied. Then the resultant initial perturbation $\psi_{0\delta}^p$ just is the CNOP. Thus, we turn a maximization problem into a minimization problem, finally obtaining the CNOP by solving this minimization problem using the SPG2 algorithm with the relevant gradient.

4. The CNOP of the SSHA forecasting

In this section, we will clarify the influence of the accuracy of mesoscale eddies in the initial field on the forecast uncertainties of oceanic state SSHA by using the CNOP approach. To do so, we adopted the SSHA-based eddy identification algorithm shown in appendix A. As an example, we plot in Fig. 1 the distribution of identified mesoscale eddies when the QG model was integrated to the time T_0 (see section 4a) starting from the initial value represented by a matrix comprised of random numbers satisfying the normal distribution $N(0, 1)$ of ψ . The flow field in Fig. 1 is dominated by a population of self-organized coherent vortices with irregular shapes and asymmetric structures of the flow field (also see Fig. 2). By statistics, these vortices have an average radius of approximately 120 km, which agrees with the statistics on the sizes of mesoscale eddies according to global SSHA observations (see Chelton et al. 2011) and represents a total of 57 mesoscale eddies. This result indicates that the two-layer QG model and

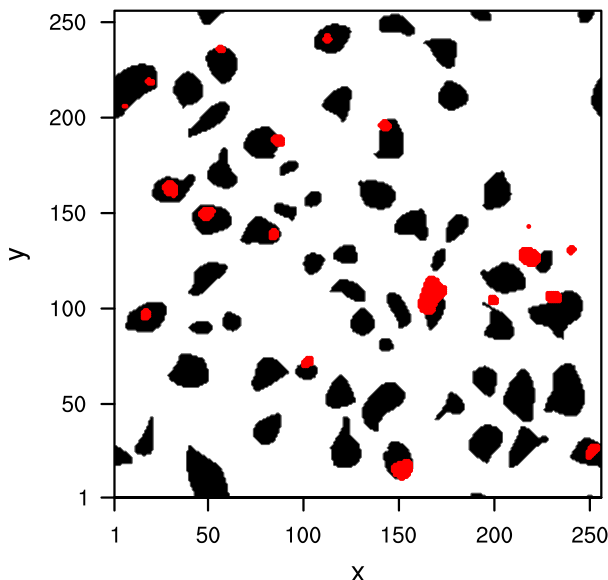


FIG. 2. The CNOP of the 7-day evolution of SSHA with the initial value is shown in Fig. 1, but only the areas occupied by the top 600 grid points with large perturbation amplitudes are colored in red. The locally distributed black areas represent different mesoscale eddies.

the approach to identifying eddies are acceptable for the theoretical study of mesoscale eddies.

a. The CNOP of the SSHA forecasts

The two-layer QG model, as mentioned above, was integrated to the time T_0 starting from the initial matrix comprised of a group of random numbers. Then, with the streamfunction ψ_i ($i = 1, 2$) at time T_0 as the initial value, the QG model was further integrated to time T_1 with $T_1 > T_0$. The duration between T_0 and T_1 was 7 days (i.e., one week), where the time integral $[T_0, T_1]$ corresponds to the 350th week in the QG model integration. With the time-dependent evolution of the SSHA during different weeks as reference states to be predicted, we calculated the CNOPs of the initial SSHA, where the initial perturbation and its final state were cared only for the SSHA ψ_1 but over the full-field model scope. The SPG2 algorithm for calculating CNOPs, as mentioned in section 3, requires the gradient information of the cost function with respect to initial perturbations, where the gradient was often calculated by integrating an adjoint model more efficiently. However, the QG model here does not have its adjoint ready, then we intend to calculate the gradient using approach of numerical derivatives. The full-field SSHA includes 65 536 grid points, which indicates a large number of perturbation dimensions and time-consuming when one uses the numerical derivatives to calculate the gradient and then the CNOP. To reduce the time costs, an empirical orthogonal function (EOF) analysis was applied to an SSHA time series taken from the 200th week to the 500th week generated by the two-layer QG model. Specifically, we took the SSHA at the first day of each week and formed the time series of

SSHA. Then a data matrix Ψ of 65 536 rows and 301 columns was obtained. If one performs the EOF decomposition to this matrix directly, a large amount of computer memory is required and it is almost impossible to obtain the EOF modes. Therefore, in the present study, we first calculated eigenvalues $\lambda = (\lambda_1, \lambda_2, \dots, \lambda_{301})$ and eigenvectors \mathbf{V}_R of the matrix $\Psi^T \Psi$, then the EOF modes of Ψ can be easily obtained by calculating the eigenvectors of $\Psi \Psi^T$ through $\mathbf{V}_N = (1/\sqrt{\Lambda}) \Psi \mathbf{V}_R$, where Λ is the diagonal matrix consisting of diagonal elements $\lambda = (\lambda_1, \lambda_2, \dots, \lambda_{301})$. For more details of this EOF decomposition, readers can be referred to Lagerloef and Bernstein (1988). Thus, the leading 50 EOF modes with a 96.92% explained variance were selected. These EOF modes can be regarded as a group of base vectors of initial perturbations of the SSHA. Then an initial perturbation $\psi_{1,0}^p$ can be formulated as follows:

$$\psi_{1,0}^p = c_1 \text{EOF}_1 + c_2 \text{EOF}_2 + c_3 \text{EOF}_3 + \dots + c_{50} \text{EOF}_{50}, \quad (10)$$

where $\mathbf{C} = (c_1, c_2, c_3, \dots, c_{50})$ are 50 constant coefficients. Different coefficients correspond to different initial perturbations, which then transfers the problem of searching for CNOP of the SSHA with 65 536 perturbation dimensions into the one searching for a particular combination of the 50 coefficients by the SPG2. With this strategy, the CNOPs of the reference states can be much easily obtained by the SPG2 with the gradient of the cost function with respect to these coefficients calculated by numerical derivatives $[J(c_k + \Delta c_k) - J(c_k)]/\Delta c_k$, $k = 1, 2, 3, \dots, 50$, with a small coefficient perturbation $\Delta c_k = 10^{-5}$.

We randomly assigned 10 reference states (i.e., ten 7-day evolution of SSHA in the model integration) to calculate the CNOPs. In addition, a total of 10 CNOPs were obtained. We found that the large perturbations of the CNOPs are locally distributed over the space; especially, the grid points of large perturbations of CNOPs are often located on mesoscale eddies. Specifically, approximately 95% of the top 600 grid points fell on some mesoscale eddies (see Fig. 2 as an example) due to sensitivity of the mesoscale eddies themselves (see sections 4b and 4c). Note that the initial perturbations in the area of large values of CNOPs may contribute more to the growth of CNOPs. It was therefore implied that the perturbation growth of the SSHA was more sensitive to the initial perturbations superimposed on the mesoscale eddies; if it was a forecast of the SSHA, its uncertainties would be highly sensitive to the initial accuracy of mesoscale eddies. Therefore, the initialization of mesoscale eddies was important to the forecasting accuracy of ocean states described by the SSHA. This result supports the perspective proposed by Weiss and Grooms (2017) that assimilating observations taken over mesoscale eddies was more effective than assimilating a subset of observations on a regular and equispaced grid covering model scope. In Weiss and Grooms (2017), the observations on evenly distributed regular grids over eddies were assimilated (also see the introduction). However, when considering the irregular shapes and asymmetric flow field of the eddies and their nonlinear evolutionary

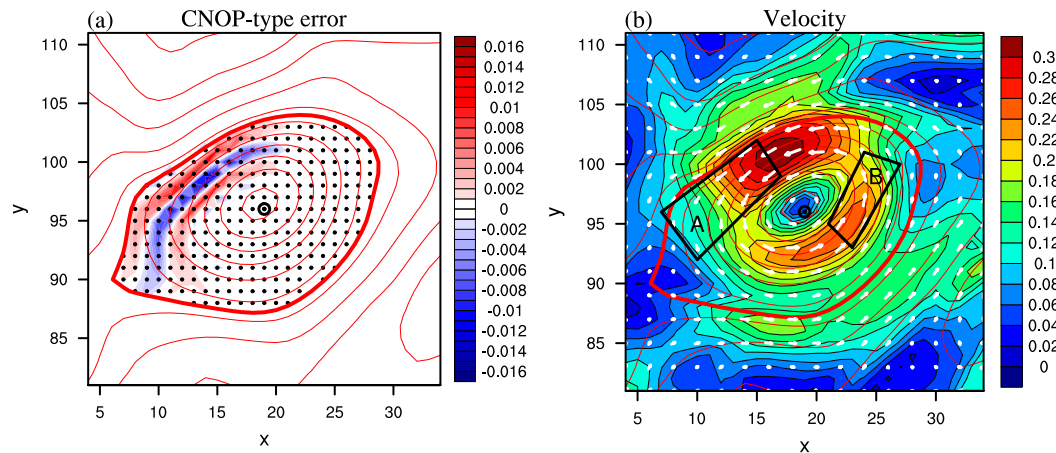


FIG. 3. (a) The CNOP-type error (shaded; m) superimposed on the initial mesoscale eddy represented by (b) the velocity (shaded; m s^{-1}), which is associated with the 7-day SSHA forecast. In (a) and (b), the black “o” represents the center of the initial eddy, the red contours outline the SSHA component, and the thick contours denote the edge of the eddy, while the white arrows in (b) represent the velocity vector. Boxes A and B in (b) denote the areas where $\partial \bar{V} / \partial t < 0$ is satisfied, with box A presenting denser contours of velocity.

behaviors, we inferred that there may exist areas over the eddies where the observations should be preferentially rearranged to be unevenly distributed and assimilated, which may improve the forecasting ability of ocean states. To confirm this inference, we next explored the CNOP-type initial errors superimposed on individual eddies for associated SSHA forecasts.

b. The CNOPs of initial eddies associated with SSHA forecasting

The CNOP, as mentioned above, represents the initial perturbation that caused the largest perturbation growth. The growth of the CNOP was more sensitive to the initial perturbations in the area of large CNOP values. Such an area may represent the sensitive area of perturbation growth with respect to initial perturbations. In this situation, the forecasting accuracy can be significantly improved by reducing the initial errors in the sensitive area identified by the CNOP. Therefore, to initialize the mesoscale eddies much better and improve the forecast level of the SSHA, it is necessary to explore the sensitive area of mesoscale eddies by using the CNOP method. As an initial attempt, we focused on individual mesoscale eddies and explore their sensitive area for improving the forecast level of their associated SSHA. Since the individual eddies cover a much smaller number of grids (at most 1000 grids; see appendix A) and have much lower perturbation dimensions for computing the optimally growing initial errors, we directly computed the gradient of the cost function with respect to initial perturbations superimposed on individual initial eddies using numerical derivatives rather than that with respect to coefficients of EOF modes.

For the predetermined 57 eddies in Fig. 1, the CNOP-type initial error of each individual eddy was calculated for the SSHA forecast with a lead time of 7 days, and a total of 57 CNOP-type errors were obtained, where the SSHA to be predicted was prescribed as a rectangle that covers the area occupied by the initial eddy and its final location after a 7-day evolution. By observing the initial errors of CNOP-type, most

of them (specifically, 39/57) possessed common features. Furthermore, this feature was found to be independent of the size of the rectangle covering the initial eddy and its final location after a 7-day evolution. These CNOP-type errors generally presented their dominant errors in the area where the initial eddies present an apparent velocity gradient from high to low speed along the eddy rotation and often had a shear structure of the SSHA there (see Fig. 3 for an example of CNOPs). Other CNOP-type errors did not show this feature; in particular, they yielded much smaller forecasting errors of SSHA, which, by comparison and inferentially, is resulted from the corresponding initial eddy failing to have an obvious velocity gradient and being unable to induce the unstable shear structure of initial errors favoring large prediction errors (also see section 4c). This finding indicated that the SSHA forecasts are less sensitive to the accuracy of the initial eddies without an obvious velocity gradient, which may illustrate why the large perturbations of the CNOPs over the full-field domain for the SSHA forecasts are locally distributed on some mesoscale eddies rather than on others. That is, the initial uncertainties of these eddies are much more weakly disturbing the SSHA forecasts. For this reason, we do not care here them but preferentially pay attention to the initial eddies of obvious velocity gradients.

c. Interpretation

As shown above, CNOP-type errors generally occur in the area where the initial eddies present an obvious velocity gradient from high to low speed and often present a shear structure of the SSHA, causing aggressively large prediction errors of the SSHA. In the present section, we interpret why the CNOPs have these features.

This problem is equivalent to understanding why the CNOPs with those features mentioned previously can significantly grow. To address this issue, we adopted the approach of eddy-energies analysis (Tsuji no et al. 2006; Fujii et al. 2008). Generally, the calculation of eddy energies requires the

decomposition of an instantaneous flow field into a mean flow and an eddy fluctuation, where the mean flow is often defined as the long-term mean of the instantaneous flow field, so in general, the eddy fluctuation is obtained by subtracting the mean flow from the instantaneous flow and bears temporal and spatial variability. For a horizontal mean flow, the growth of the eddy fluctuation often results from the barotropic instability of the mean flow. The kinetic energy for supporting the growth of the eddy fluctuation comes from the mean flow. The kinetic energy of the mean flow transitioning to the eddy fluctuation can be measured by a barotropic conversion rate (BT), which can be derived by the following Eq. (11) [i.e., the tendency equation of eddy kinetic energy (EKE) under the quasigeostrophic assumption]:

$$\frac{\partial \text{EKE}}{\partial t} = -\rho_0 \left[u' u' \frac{\partial \bar{u}}{\partial x} + u' v' \left(\frac{\partial \bar{u}}{\partial y} + \frac{\partial \bar{v}}{\partial x} \right) + v' v' \frac{\partial \bar{v}}{\partial y} \right] + \text{residue}, \tag{11}$$

where \bar{u} and \bar{v} are zonal and meridional velocities of the mean flow; u' and v' are the corresponding velocities of the eddy fluctuation field, respectively; and

$$\text{BT} = -\rho_0 \left[u' u' \frac{\partial \bar{u}}{\partial x} + u' v' \left(\frac{\partial \bar{u}}{\partial y} + \frac{\partial \bar{v}}{\partial x} \right) + v' v' \frac{\partial \bar{v}}{\partial y} \right]. \tag{12}$$

Obviously, the EKE can be converted from the mean flow only when the BT is positive.

For particular physical problems of concern, there may exist various definitions of mean flow and eddy fluctuation. Despite this, the BT can also be regarded as an indicator of barotropic instability (see Fujii et al. 2008). In the present study, the reference state to be predicted can be treated as the mean flow, and the CNOP-type errors are regarded as the eddy fluctuation. The BT for the evolution of the CNOP-type errors can be calculated. A positive BT always occurs in the area occupied by large values of CNOP-type errors, i.e., the area where the initial eddies of the reference state present an obvious velocity gradient from high to low speed. Figure 4 plots the BT of the CNOP-type error shown in Fig. 3. The initial errors in the area where the initial eddies present an obvious velocity gradient from high to low speed are more likely to extract energy from the reference state and grow significantly. Why does the positive BT tend to occur in this area?

To answer the above question, we can rewrite the BT as in Eq. (13) (the derivation can be seen in appendix B), which is established under the frame of a natural coordinate system and uses the Lagrange expression, which is calculated as follows:

$$\text{BT} = -\frac{V'^2}{(\bar{V} + V')} \frac{\partial \bar{V}}{\partial t}, \tag{13}$$

where V' is the velocity in the CNOP-type error and its evolution, and $\bar{V} > 0$ in the natural coordinate system and represents the velocity in the reference state with $|V'| < \bar{V}$ generally. We split Eq. (13) into two terms $-V'^2/(\bar{V} + V')$ and $\partial \bar{V}/\partial t$. Clearly, a larger $|V'|$ will result in the term $-V'^2/(\bar{V} + V')$ having a larger absolute value, which

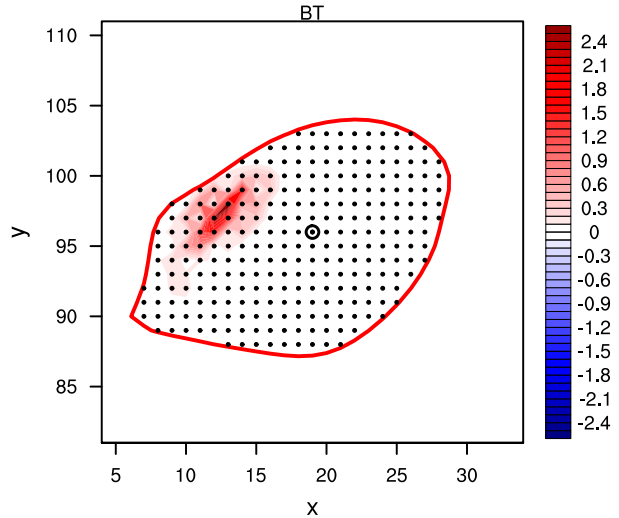


FIG. 4. The distribution of the BT ($10^{-7} \text{ m}^2 \text{ s}^{-3}$) of the CNOP-type error in Fig. 3. The dots occupy the eddy, with the red bold line denoting the eddy edge.

indicates that the BT is larger in absolute value and that more energy can be converted. Since the trace line on the vortex is approximately circular, $|V'| = |\partial \psi' / \partial r|$ can be approximately deduced (see appendix C). Therefore, a large $|V'|$ corresponds to a large $|\partial \psi' / \partial r|$. Thus, if and only if the CNOP-type errors possess the strongest positive–negative contrast of perturbed SSHA, as in Fig. 3a, they can yield the largest velocity $|V'|$ and then the most energies are converted. This finding explains why the CNOP-type errors tend to have a shear structure of ψ'_1 , as shown in Fig. 3a.

Since the velocities generally satisfy $|V'| < \bar{V}$, the term $-V'^2/(\bar{V} + V')$ is often negative. Therefore, when the term $\partial \bar{V}/\partial t$ is also negative, the BT can be positive. In Fig. 5, the 7-day evolution of the SSHA and velocity, followed by Euler expression, always exhibits an eddy structure similar to the initial eddy, whereas the water masses on the eddy, followed by Lagrange expression, are simultaneously in motion. Then, $\partial \bar{V}/\partial t$ mainly reflects the velocity tendency of the water masses in the eddy. With the initial eddy shown in Fig. 3, we integrate the QG model and calculate $\partial \bar{V}/\partial t$ at different times. There are always two locations on the eddy (marked by boxes “A” and “B”), which satisfy $(\partial \bar{V}/\partial t) < 0$; in particular, the velocities in box A present much denser contours, implying that the term $\partial \bar{V}/\partial t$ in box A is more negative, which, combined with the term $-V'^2/(\bar{V} + V')$, enhances the BT more positive in box A. The $\partial \bar{V}/\partial t < 0$ and its induced positive BT means that in the areas with the water mass velocity of the eddy changing from large to small, the initial errors have the potential to extract more energies and develop into larger errors. Thus, the initial errors occurring in box A are inclined to grow much more significantly, which indicates the CNOP-type errors, as the initial perturbation that has the largest nonlinear growth, preferentially occurring in the area where the initial eddy presents a large velocity gradient with the velocity decreasing along the rotation direction of the

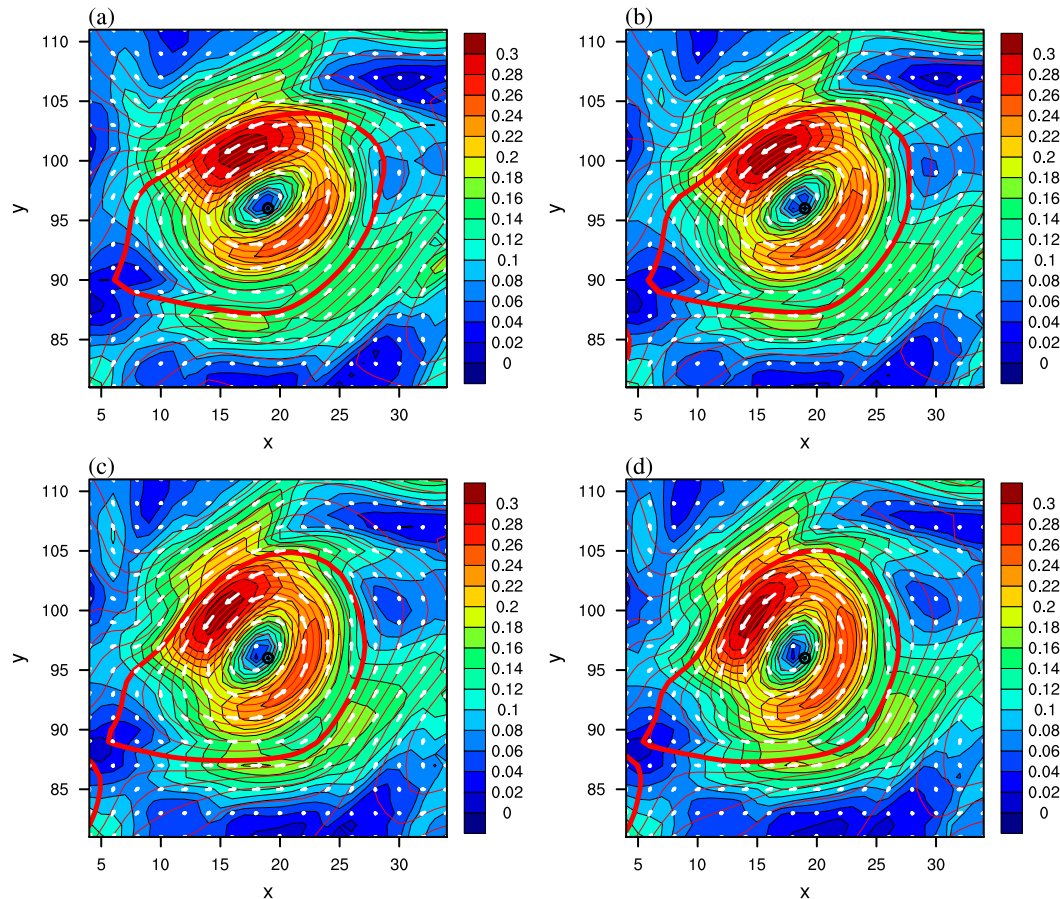


FIG. 5. The evolution of the SSHA with the initial eddy as in Fig. 3b. The velocity (m s^{-1}) is plotted in for the time (a) T_0 , (b) $(1/3)(T_1 - T_0)$, (c) $(2/3)(T_1 - T_0)$, and (d) T_1 , where $[T_0, T_1]$ corresponds to the 350th week in the QG model integration (see section 4a). The red contours draw the outline of the SSHA fields, the thick closed contours represent the edge of the eddy, and the white arrows denote velocity vectors.

vortex. This sheds light on that the CNOP-type errors of such structures are less sensitive to orientation for eddies that are more isotropic, which is also responsible for why the large perturbations of the CNOPs superimposed on the full-field domain are locally distributed on some eddies (see section 4a) and other eddies do not present their own CNOP-type errors as of an obvious shear structure of SSHA (see section 4b).

5. Sensitivity to CNOP-type errors superimposed on initial eddies

In the last section, we illustrated the CNOP-type errors of the SSHA forecasting tend to be located on the initial eddies and are especially concentrated in the areas with an obvious velocity gradient from high to low speed; furthermore, the CNOP-type errors often present a shear structure of the SSHA there. Physically, we have explained the rationality of the CNOP-type errors as the optimally growing initial errors superimposed on the initial eddy associated with the SSHA forecasts. As analyzed above, the growth of CNOP-type errors is more sensitive to the errors in the areas

in which the CNOP-type errors concentrate and have large error values. These areas may represent the sensitive areas of initial eddies for target observations associated with SSHA forecasts; then, the forecasting accuracy could be significantly improved by reducing the initial errors in the sensitive areas. To confirm this inference, we conducted the following two groups of numerical experiments to show the sensitivity of SSHA forecasting errors to CNOP-type errors.

a. Sensitivity to locations of initial eddy errors

We first explored the sensitivity to the locations of initial eddy errors. Five groups of experiments, denoted as R1, R2, R3, R4, and R5, were predesigned (see Fig. 6). The groups of experiments investigated the effect of possible observational errors on 16 different grid points on the initialization of mesoscale eddy. To do so, we superimposed the initial perturbations on the 16 grid points when they were located in the sensitive area in R1 and that of the nonsensitive areas in R2–R4. In R5, the 16 grid points have a uniform distribution over the mesoscale eddy, similar to Weiss and Grooms (2017). For each of R1–R5, we generated 25 groups of

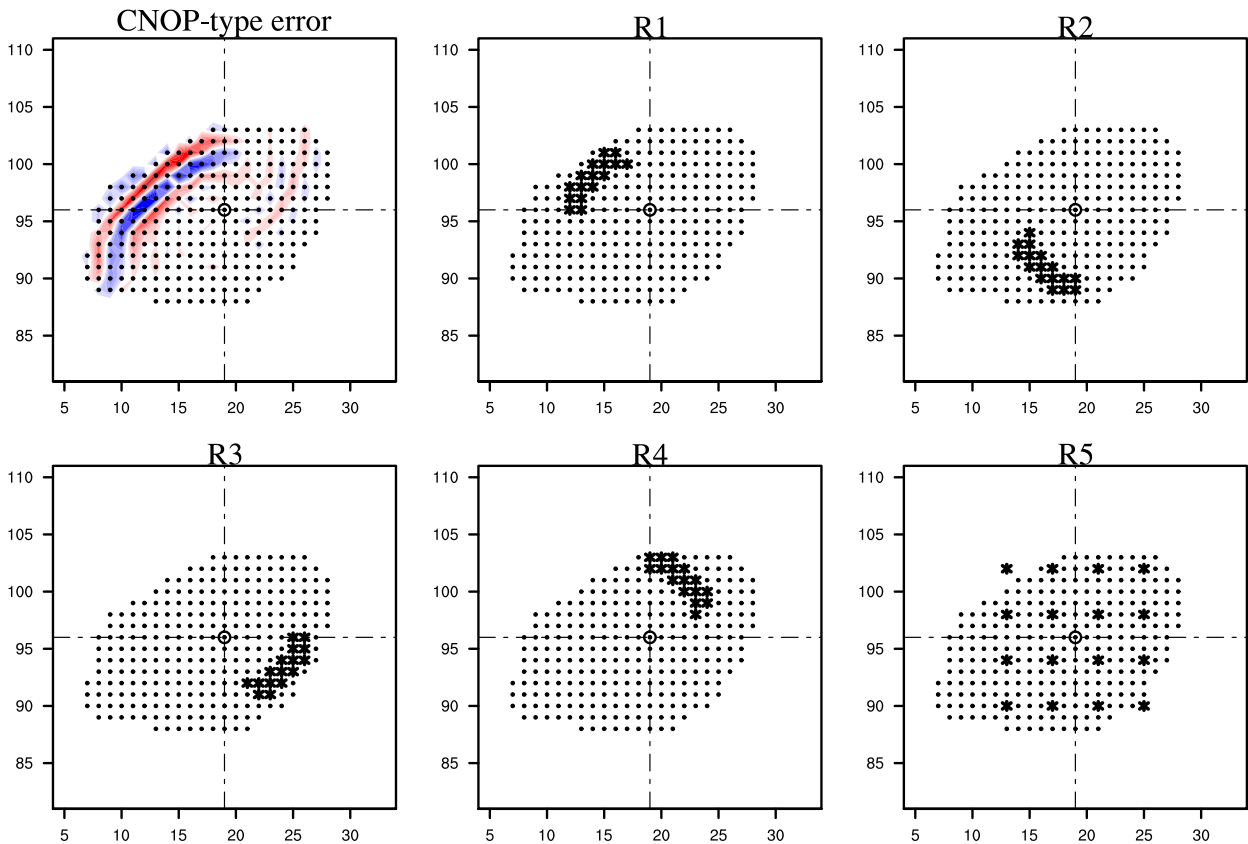


FIG. 6. R1, R2, R3, R4, and R5 show separate experiments, where 16 different grid points on the mesoscale eddy (shown in Fig. 3b) are selected and initial errors are superimposed. The black stars denote the 16 grid points, and the black “○” represents the center of the initial eddy. The 16 grid points in R1 occupy the area where CNOP-type error is located, i.e., the sensitive area of the eddy.

random initial errors with the random number at each grid of a normal distribution $N(0, \sigma_1)$, where σ_1 is a positive number and prescribed as being stochastically yielded from the interval (0, 4) when considering the amplitude of observational error. With these initial errors, the QG model was integrated for 7 days to obtain the SSHA forecasts.

We took the differences between the SSHA forecast result and the reference state SSHA and obtained the forecast errors of the SSHA caused by the 25 random initial errors in R1–R5. Figure 7a shows these forecast errors. The forecast errors that occurred in R1 were generally significantly larger than those in R2–R5. This finding showed that the forecast errors of the SSHA was more sensitive to the random initial errors in the sensitive area identified by the CNOP-type errors than in other areas.

b. Sensitivity to spatial structures of initial eddy errors

Further, we compared the forecast errors caused by 25 groups of random initial errors with those caused by the CNOP-type errors. The R1–16 gridpoint (i.e., the 16 grid points in R1) component of the CNOP-type initial errors tended to yield much greater forecast errors compared with the random initial errors in R1 when they are scaled to have the amplitude of the R1–16 gridpoint component of the

CNOP-type error (see Fig. 7b). The CNOP-type errors and random initial errors presented different spatial structures. It can therefore be inferred that the spatial structure of initial errors plays an important role in yielding a large forecast error. To further examine this perspective, we conducted the following sensitivity experiments.

Based on the above 25 groups of random initial perturbations in R1 and the R1–16 gridpoint component of the CNOP-type error, we generated new types of initial errors of special patterns as follows:

$$\text{Type}_\alpha = \alpha \text{CNOP-type error} + (1 - \alpha) \times \text{random error}, \quad (14)$$

where $\alpha = 0, 0.1, 0.2, 0.3, \dots, 1$. Obviously, these errors also occur on the 16 grids in R1. With increasing α , the new type of error bears increasing similarities to the CNOP-type error. For a fair comparison, all new types of initial errors were scaled to have an amplitude similar to that of the CNOP-type error. With these new initial errors, the forecast errors of the final SSHA were investigated. Figure 7b displays a box plot for the forecast errors caused by 25 groups of new initial errors for each value of α . It is shown that the forecast errors become increasingly larger with increasing α . In fact, the new errors, as mentioned above, are similar to CNOP-type errors

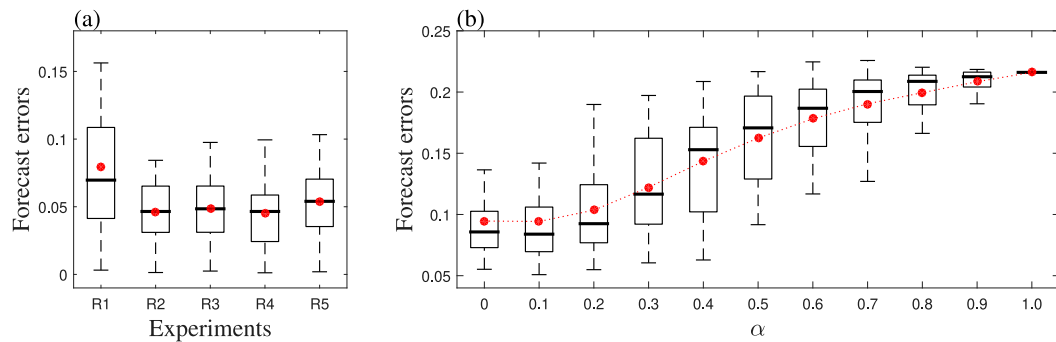


FIG. 7. The boxplot of the forecast errors (m) caused by (a) 25 random initial errors in the area shown in R1–R5 and (b) the initial errors of the special patterns characterized by the coefficient α in R1. The red bold dots represent the mean value, and the black bold lines denote the median. Particularly, the red bold dot with $\alpha = 0$ corresponds to 25 random initial errors, while that with $\alpha = 1.0$ corresponds to the CNOP-type initial error.

when α is large. Therefore, we confirmed that the initial errors of a particular structure in sensitive area R1, as shown in CNOP-type errors, are more likely to cause larger forecast errors than other initial errors.

It is noted that the experiments in section 5a and 5b took the eddy shown in Fig. 3 as an example to show the sensitive area and its associated unstable structures of initial errors. In fact, for all the 39 eddies whose CNOP-type errors coincide with the unified characteristics summarized in section 4b, we conducted similar experiments and consistent results are obtained. That is, the SSHA forecasting uncertainties are very sensitive to the initial errors in the sensitive area over the initial eddies, especially to those of particular unstable structures, as in the CNOP-type errors. This finding indicates that if additional observations, especially with a particular array indicated by the CNOP-type errors, are preferentially implemented in the sensitive areas over the eddies and assimilated, the forecasting ability of the SSHA could be greatly improved.

6. Observing system simulation experiments to confirm the rationality of sensitive area for target observation

In this section, we conducted observing system simulation experiments (OSSEs) to confirm the rationality of the sensitive area determined by CNOP-type errors. To do so, we took the reference state from T_0 to T_1 to represent the “true” state (hereafter “Nature Run”) and generated synthetic or pseudo observations by adding errors on Nature Run at selected observation sites. Based on the Nature Run, we superimposed white noise with different amplitudes of variances on the Nature Run at time T_0 and then performed the Lanczos filtering algorithm to make the flow fields smooth. With these flow fields as initial values, we integrated the QG model to time T_1 (see section 4a) and obtain various “Control Run” or control forecasts of the Nature Run.

Different control forecasts will have separate forecast errors, which, are caused by various initial errors, i.e., the differences between the Nature Run and Control Runs at time T_0 (see section 4a). Certain initial errors will lead to significant forecast errors, whereas others will yield negligible

forecast errors. For the initial errors causing negligible forecast errors, the forecast results have been satisfying, and even if the targeted observations are assimilated, the improvement of the forecast result is indistinguishable. Therefore, to evaluate the effect of target observations more reasonably, we chose control forecasts with large forecast errors to conduct assimilation experiments on target observations. Specifically, we generated 100 Control Runs of the Nature Run and considered the corresponding 100 initial errors. These initial errors were all scaled to have the same amplitude by $\mathbf{X}'_i = \lambda_i \mathbf{X}_i$, where \mathbf{X}_i and \mathbf{X}'_i ($i = 1, 2, 3, \dots, 100$) denote the initial error of the Control Run and its scaled counterpart, respectively; λ_i denotes the scaling factor, which should make \mathbf{X}'_i satisfy

$$\sqrt{\frac{N}{\sum_{i,j=1}^N (\mathbf{X}'_{i,j})^2}} / N = (1/5)\delta_0,$$

where δ_0 is the standard deviation of the initial SSHA in the 10 reference states (see section 4a), j denotes a grid point, and N represents the total number of grid points in the rectangle that covers the area occupied by the initial eddy and its final location after a one-week evolution. The forecast errors caused by the initial errors are all examined, and the top 30 initial errors with large forecast errors were selected for conducting the OSSEs.

In the OSSEs, the synthetic observations were assimilated into the initial field of the Control Run and formulated a new initial field. With this new initial field, we integrated the QG model and obtained a new forecast with respect to the SSHA. For convenience, we referred to this new forecast as the “Assimilation Run.”

For the 39 eddies whose CNOP-type errors can identify the sensitive area for SSHA forecasting (see section 4b), we adopted the above strategy to conduct OSSEs and showed the sensitivity of the CNOP-type errors. Since similar results are obtained, for simplicity, we only use the eddy in Fig. 3 to describe the result. In the Assimilation Run, five different assimilation strategies were used. Figure 8 shows these strategies, which are referred to as E91, E31, E32, E33, and E34. E91 means that the synthetic observations are evenly distributed on 9 grids over the eddy (similar to Weiss and Grooms 2017) and assimilated; E31 assimilates only three (in the sensitive area; i.e., the box A in Fig. 3) of the 9 grids

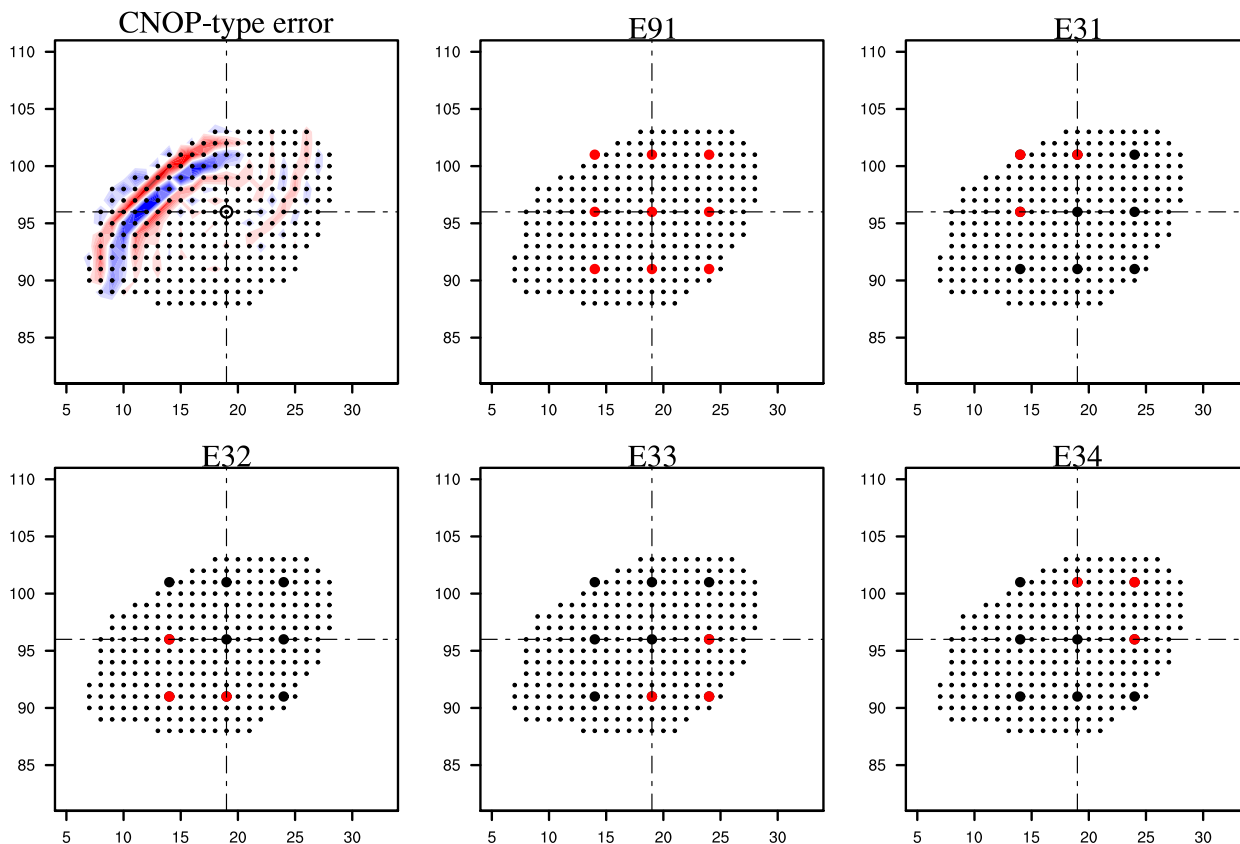


FIG. 8. CNOP-type errors and five kinds of assimilation strategies. The bold points represent the observations, and the red points indicate the observations to be assimilated.

in E91, while E32, E33, and E34 assimilate another three that do not fall in the sensitive area (see Fig. 8). Note that the E34 almost corresponds to the box B in Fig. 3. Optimal interpolation (see appendix D) was employed to assimilate synthetic observations. The benefits of the SSHA forecasting skill from assimilating observations were evaluated by Eq. (15):

$$b = \frac{dF_1 - dF_2}{dF_1} \times 100\%, \quad (15)$$

where dF_1 is the forecast error of the Control Run with respect to the Nature Run and dF_2 is the forecast error of the Assimilation Run with respect to the Nature Run.

With these assimilation strategies, we integrated the QG model and calculated the benefits from assimilating target observations. The ratio between the benefits b of $E3i$ ($i = 1, 2, 3, 4$) and that of E91 are calculated and then plotted in Fig. 9, which measures the contribution of assimilating three observations to the improvement of the forecast ability of the SSHA when assimilating the nine observations. E31 had the largest contribution. Furthermore, there respectively exist one grid observation in E32 and E34 overlaps with the observations in E31. That is, the locations of the observations in E32 and E34 are very close to the sensitive area; consequently, E32 and E34 presented secondarily large contributions to the improvement of

the forecast ability of the SSHA. From these experiments, we confirmed that preferentially implementing additional observations in the sensitive area determined by CNOP-type errors is indeed valid for improving the initialization of mesoscale eddies and then the associated forecast level of the ocean state described by SSHA.

In section 5b, it was deduced that the targeting observations should also be considered with what array to display according to the sensitivity to the structure of the CNOP-type errors. To verify this point, we further conducted the following OSSEs. The assimilation strategy was essentially the same as that in the former part with the exception that the three-grid observations are randomly selected from those in the sensitive area. A total of 30 arrays for three-grid observations were obtained for each of the 39 eddies of concern (see section 4b), and a common conclusion is obtained. Figure 10 shows the 30 arrays in the sensitive area (i.e., the box A) for the eddy in Fig. 3. Here, we similarly take this eddy as an example to illustrate the results. With the assimilation of the 30 observational arrays, we calculated their benefits (see Fig. 11) and found that if and only if observations exist with an array displayed along the radial direction of the eddy, the benefits from assimilation will be notable. Such observational arrays crosscut the shear structure of the SSHA similarly as in the CNOP-type errors and are helpful for capturing the spatial characteristic of

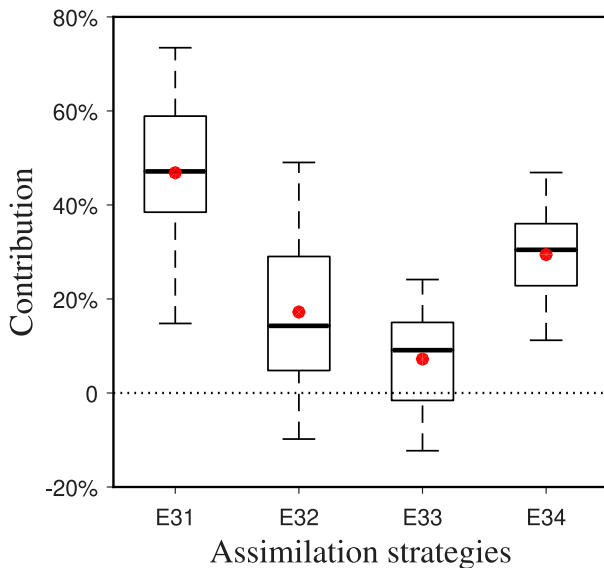


FIG. 9. Boxplot of the contribution of assimilating selected three-grid observations to the reduction in the control forecast errors when assimilating nine evenly distributed grid observations, where the associated control forecasts are the 30 Control Runs with large forecast errors.

the optimally growing initial error superimposed on the eddy, and by assimilating them we are able to effectively reduce its effect on the SSHA forecasting. It is also argued that the box B of the eddy in Fig. 3 presents strong velocity shear despite it is weaker than that in the box A and one may question how important it is for the benefits. To address it, we conducted similar OSSEs and demonstrated that the benefits from the assimilation in the box B are significantly less than those in the box A (i.e., the sensitive area), with the former being less than 20% at maximal while the latter being up to more than 30% at maximal. Furthermore, we found that the variability among the benefits made by 30 assimilation strategies for the box B are not as significant as that for box A despite the large benefits for boxes A and B are all for the observational arrays that crosscut the shear structure of the SSHA. All these demonstrated that the benefits after assimilation are more significantly sensitive to the strong velocity gradient occurring along the rotation of the initial eddy, which is responsible for the occurrence of the CNOP-type error with a shear SSHA structure there. In numerical experiments, we also tried assimilation strategies with more observations and similar results were obtained. Therefore, the structure of the CNOP-type errors provides guidance to implement target observations with what array to display. This finding also sheds light on how the evenly distributed observations as doing in Weiss and Grooms (2017) are preferentially redisplayed according to the array indicated by the CNOP-type errors, then finally improving the SSH forecasting ability.

7. Summary and discussion

Motivated by the crucial role of oceanic mesoscale eddies in influencing oceanic fluid motions and associated weather and

climate anomalies, we conducted the first attempt to investigate the optimally growing initial error of the SSHA forecasts by using the CNOP approach and illustrated the role of mesoscale eddies in improving the SSHA forecasts generated by a two-layer QG model. The results showed that in the optimally growing initial errors characterized by the CNOP, the components located on the mesoscale eddies tend to contribute more to the forecasting errors of the SSHA with a 7-day lead time, which indicated that the accuracy of the mesoscale eddies distributed over the initial SSHA field was particularly important when obtaining the high skill of the SSHA forecasts. This result coincides with the perspective proposed by Weiss and Grooms (2017) that assimilating evenly distributed observations over mesoscale eddies is more effective than assimilating a subset of observations on a regular and equispaced grid covering model scope in improving SSH forecasting ability. However, by calculating and observing the CNOP-type initial errors superimposed on individual eddies, we found that the dominant errors tend to occur at a particular location where the eddies exhibit an obvious velocity gradient from high to low speed along the rotation direction and often have a shear structure of the SSHA there. This finding implies that the initial errors at different locations over the eddy may have different contributions to the final forecast errors of SSHA and in the above particular location shows the strong sensitivity to initial errors of SSHA forecasts (note that this particular location can also be referred to as a “sensitive area”). Therefore, assimilating evenly distributed observations over mesoscale eddies in Weiss and Grooms (2017) may not be the optimal assimilating strategy for SSHA forecasting. Then, we infer that if additional observations are preferentially implemented, especially with a particular array in the above particular location, and assimilating them to the initial field, the forecasting skill of the SSHA could be significantly improved.

Physically, we interpreted the sensitivity of the CNOP-type errors superimposed on individual eddies by barotropic instability and provided theoretical evidence for the above inference on the very effective assimilation strategy of mesoscale eddies associated with SSHA forecasts. Specifically, a positive BT will ensure that the errors obtain energy from the reference state to develop. Therefore, if the eddies in the reference states have a location where the fluid exhibits the most apparent velocity gradient, with values from large to small along the rotation direction and the errors themselves possess a strong shear structure with a positive–negative contrast of SSHA, they will determine the associated BT is positive and its value is the largest. Then, most energies can be converted from the reference states to errors, finally being favorable for the errors growing optimally. Since we are finding the optimally growing initial errors superimposed on initial eddies associated with the SSHA forecasts, the resultant CNOP-type initial error, as the optimally growing initial error, must feature that its dominant errors occur at the location where the eddies exhibit an obvious velocity gradient from high to low speed along the rotation direction and often have a shear structure of the SSHA over there.

Numerically, we conducted sensitivity experiments and OSSEs to verify the sensitivity of CNOP-type initial errors

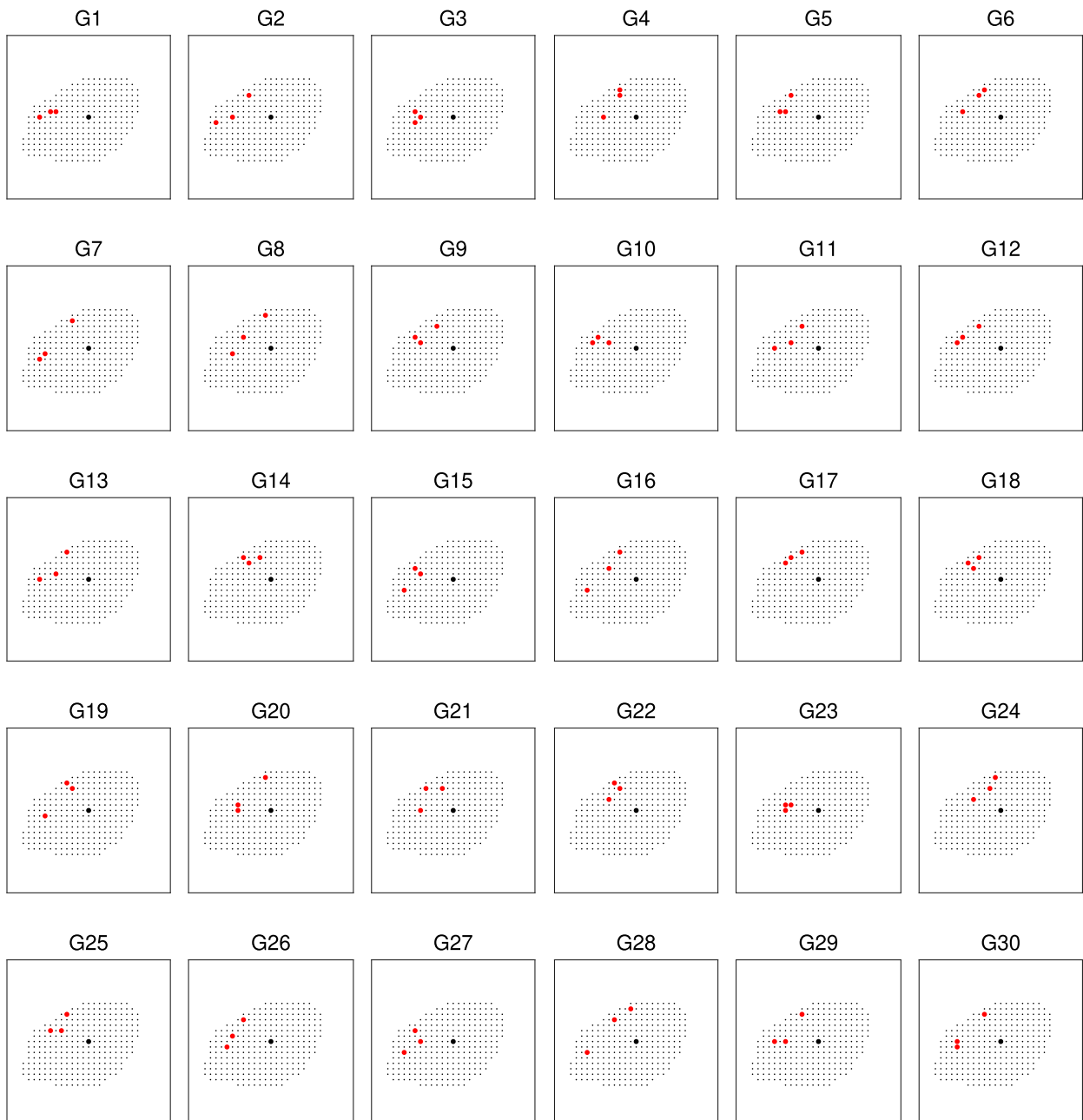


FIG. 10. G1–G30 represent 30 assimilation strategies, where the three-grid observations are randomly selected from those in the sensitive area of the eddy. The bold black dots denote the center of the eddy, and the bold red dots indicate the location of the three observations to be assimilated.

and suggest a much more effective target observation strategy of mesoscale eddies associated with SSHA forecasts. The results showed that when random initial errors are added in the sensitive area, they lead to larger forecast errors than in other regions over the mesoscale eddies; in particular, if an initial error with a structure similar to the CNOP-type initial errors is added on the initial eddies, it significantly enhances the forecast errors of SSHA. Consequently, both sensitive

areas occupied by CNOP-type errors superimposed on initial eddies in the reference states and the associated shear structure of the errors make the largest contribution to the final forecast errors of SSHA. Therefore, if additional observations are implemented in the sensitive area, especially with an array of observations that can capture the shear structure of the errors, the SSHA forecasting skill can be significantly improved by assimilating these additional observations. The

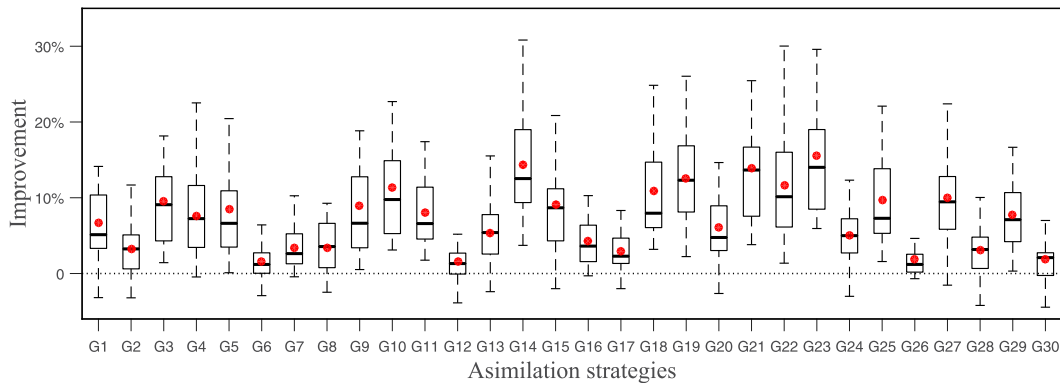


FIG. 11. Boxplot of the control forecast error reduction after assimilating selected three-grid observations in G1–G30, where the control forecasts are the 30 Control Runs with large forecast errors.

OSSEs were used to verify the above sensitivity of the CNOP-type errors. They illustrated that preferentially implementing additional observations in the sensitive area determined by the CNOP-type errors is indeed valid for improving the initialization of mesoscale eddies and then the associated forecast level of the SSHA; in particular, if and only if observations arranged along the radial direction of the eddy exist, the benefits from assimilation are considerable. Obviously, these particular observational arrays located in the sensitive area capture the shear characteristics of the optimally growing initial errors and show the usefulness of the CNOP structure in implementing targeting observations with what array to display.

In realistic field campaigns, although it is difficult to target the accurate positions to implement the additional observations due to problems of observing methods and associated observing devices and instruments, which must lead to observational errors, these observations have reflected the real world to a high degree (Mu 2013). In addition, as the first attempt at target observations of mesoscale eddies associated with SSHA forecasting, we adopted a simple two-layer quasigeostrophic model to investigate this issue. In particular, we only paid attention to the surface flow associated with individual mesoscale eddies. From the resultant CNOP sensitivity and its interpretation of barotropic instability, it seems that a much simpler shallow-water model is also applicable to the problem of concern here. Of course, this should be confirmed by a comparison between the two-layer model and the shallow-water model to identify the particular role of the two-layer model. In any case, our original intention is to implement a comparison between the present study and that of Weiss and Grooms (2017) and the two-layer QG model is finally adopted. In addition, we also realize that the mesoscale eddies in actual stratified oceans generally exhibit a three-dimensional structure and interaction among themselves, which may be related to a mixture of barotropic and baroclinic instabilities (Liao et al. 2019). In this scenario, a more practical model is expected to be useful for investigating the effect of the accuracy of mesoscale eddies on the forecasting ability of ocean states such as SSHA, even other oceanic variables, finally designing the optimal observation network of mesoscale eddies and improving the forecast level of the ocean state to a greater extent.

It is also realized that, although the simple two-layer QG mode adopted in the present study, which does not have its adjoint model ready, allows us to solve the gradient by calculating the numerical derivatives, a large amount of time cost is still required for solving CNOP. Certainly, such doing is inadvisable for complex realistic models. In fact, there exist adjoint models of some realistic models such as the Weather Research and Forecasting (WRF) Model (Michalakes et al. 2001) for weather forecasts, the Regional Ocean Model System (ROMS) (Shchepetkin and McWilliams 2005) for oceanic simulations, and others. Related to the present study, one can also use the ROMS model and its adjoint to explore the mesoscale eddy of concerned problems. Of course, there exist some intelligent algorithms, such as particle swarm optimization (PSO), genetic algorithm, etc., which have been emerging to solve high-dimensional optimization problems. These algorithms do not calculate the gradient and may be applicable to models of different complexities. It is therefore expected that such kind of algorithms can be applied to calculate the CNOP for more realistic models and further explore sensitivity of mesoscale eddies in the future.

Acknowledgments. The authors are very grateful to the two anonymous reviewers and Prof. Konstantin Belyaev from Shirshov Institute for Oceanology, RAS, and Lomonosov Moscow State University, Faculty computational Math and Cybernetics for their highly complimentary remarks to the study and constructive suggestions. The authors also thank Prof. Jeffrey B. Weiss very much for his providing the two-layer QG model adopted in the present study. The study was jointly supported by the National Key Research and Development Program of China (2018YFC1506402) and the National Natural Science Foundation of China (Grants 41930971 and 41525017).

Data availability statement. The datasets generated and/or analyzed during the study are stored on the computers at State Key Laboratory of Numerical Modeling for Atmospheric Sciences and Geophysical Fluid Dynamics (LASG; <https://www.lasg.ac.cn>) and will be available to researchers upon request.

APPENDIX A

Vortex Identification Algorithm

The present study adopts the SSHA-based eddy identification algorithm suggested by Chelton et al. (2011) to determine the vortex position. Then, a mesoscale eddy can be defined as a connected set of grids that satisfy the following criteria:

- 1) The values of the SSHA on the grids are above (or below) a given threshold for anticyclonic (cyclonic) eddies.
- 2) There are at least 20 grids but fewer than 1000 grids comprising the connected region.
- 3) There exists one local maximum (minimum) of the SSHA for anticyclonic (cyclonic) eddies.

In the present study, the threshold above is prescribed as 1.5 times the RMS (root-mean-square) of the SSHA field over the whole model scope. With this threshold, the locations of the eddies are approximately determined, and then the outermost closed contour of the SSHA for each eddy can be sketched as the eddy edge according to the second and third criteria.

APPENDIX B

Calculation of BT in the Natural Coordinate System

The natural coordinate system here is established along the trace of the water mass, where the tangent and normal directions (denoted by \mathbf{s} and \mathbf{n}) of the trace are two coordinates of the system. Through the quasigeostrophic (QG) balance assumption, a flow can be decomposed into a leading-order geostrophic flow component V and a small ageostrophic component V_a . The geostrophic flow satisfies Eq. (B1):

$$f_0 V = -\frac{1}{\rho} \frac{\partial p}{\partial n}, \tag{B1}$$

where f_0 is the Coriolis parameter, ρ is the density, and p is the pressure.

The variability of the geostrophic flow V is controlled by the next-order momentum (Tsujino et al. 2006) and is described as follows:

$$\frac{V^2}{R} = -f_0 V_a - \frac{1}{\rho} \frac{\partial p_a}{\partial n}, \tag{B2}$$

where R is the curvature radius and p_a is the small ageostrophic component of pressure. The calculation of eddy energies requires decomposition of instantaneous fields into mean and eddy fluctuation fields, where the mean field is often defined as a long-term mean (denoted by a bar) and its eddy fluctuation (denoted by a prime) is defined as the deviation from it. The following Eq. (B3) shows the decomposition of the relevant variables:

$$V = \bar{V} + V', \quad V_a = \bar{V}_a + V'_a, \quad p_a = \bar{p}_a + p'_a. \tag{B3}$$

Substituting Eq. (B3) for Eq. (B2), it is derived as follows:

$$V'^2 = -f_0 R V'_a - 2\bar{V} V' - \frac{R}{\rho} \frac{\partial p'_a}{\partial n}. \tag{B4}$$

By seeking a partial derivative with respect to time to the left and right sides of Eq. (B4), it obtains the following Eq. (B5):

$$\frac{\partial(V'^2)}{\partial t} = -f_0 R \frac{\partial V'_a}{\partial t} - 2 \frac{\partial(\bar{V} V')}{\partial t} - \frac{R}{\rho} \frac{\partial}{\partial t} \left(\frac{\partial p'_a}{\partial n} \right). \tag{B5}$$

By multiplying the left and right sides of Eq. (B5) by 1/2 and with the EKE being $(1/2)V'^2$, the control equation of the EKE can be obtained as in Eq. (B6):

$$\begin{aligned} \frac{\partial \text{EKE}}{\partial t} = & -\frac{V'^2}{(\bar{V} + V')} \frac{\partial \bar{V}}{\partial t} - \frac{f_0 R V'}{2(\bar{V} + V')} \frac{\partial V'_a}{\partial t} \\ & - \frac{V' R}{2\rho(\bar{V} + V')} \frac{\partial}{\partial t} \left(\frac{\partial p'_a}{\partial n} \right). \end{aligned} \tag{B6}$$

Clearly, the first term on the right side of Eq. (B6), i.e., Eq. (B7), is the BT, which is defined as follows:

$$\text{BT} = -\frac{V'^2}{(\bar{V} + V')} \frac{\partial \bar{V}}{\partial t}. \tag{B7}$$

APPENDIX C

The Relationship between the Streamfunction and Water Mass Velocity in the Natural Coordinate System

The trace on the vortex can be roughly regarded as a circle and approximately coincides with the streamline of water mass motion. The relationship between the natural coordinate system and the Cartesian coordinate system with the two coordinates x and y can be constructed as follows via the polar coordinate system (Fig. C1).

In Fig. C1, taking the red dot in the second quadrant as a mass point on the cyclonic vortex can be derived as follows:

$$\begin{cases} V^2 = u^2 + v^2 \\ u = -\sin\theta \times V, \\ v = \cos\theta \times V \end{cases}, \quad \begin{cases} r^2 = x^2 + y^2 \\ x = \cos\theta \times r, \\ y = \sin\theta \times r \end{cases}, \quad \begin{cases} u = -\frac{\partial\psi}{\partial y} \\ v = \frac{\partial\psi}{\partial x} \end{cases},$$

$$\frac{\partial\psi}{\partial r} = \frac{\partial\psi}{\partial x} \frac{\partial x}{\partial r} + \frac{\partial\psi}{\partial y} \frac{\partial y}{\partial r} = \frac{\partial\psi}{\partial x} (\cos\theta) + \frac{\partial\psi}{\partial y} (\sin\theta)$$

$$= \frac{\partial\psi}{\partial x} \left(\frac{v}{V} \right) + \frac{\partial\psi}{\partial y} \left(-\frac{u}{V} \right) = \frac{1}{V} [v(v) + u(u)] = V,$$

where V is the horizontal velocity in the natural coordinate system, u, v is its zonal and meridional components of V , and r is the polar radius of the polar coordinate system, which is also the normal coordinate in the natural coordinate system. The above derivations can also be done for the mass points in other quadrants, and $V = \partial\psi/\partial r$ is obtained. These derivations can similarly do for anticyclonic vortices, and V

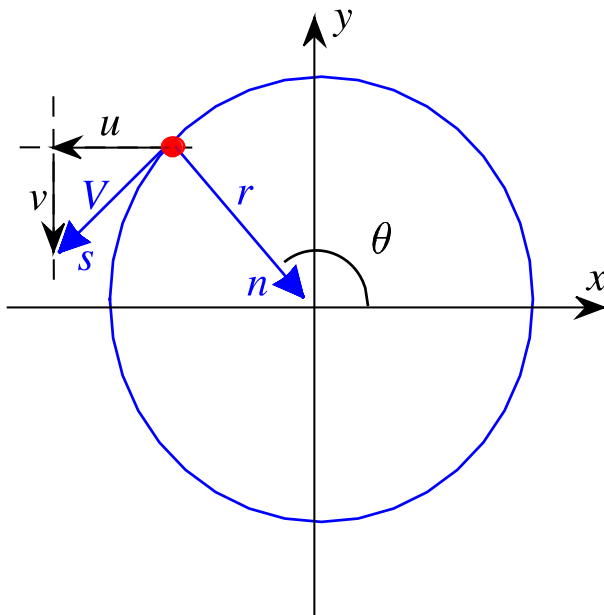


FIG. C1. Sketch map showing the relationship between the natural coordinate system with the two coordinates s , n and the Cartesian coordinate system with the two coordinates x , y via the polar coordinate system.

$= -\partial\psi/\partial r$ is obtained. Therefore, the relationship between the streamfunction and velocity of the mass points on the vortex can be expressed as $|V| = |\partial\psi/\partial r|$.

APPENDIX D

Optimal Interpolation Assimilation Approach

The optimal interpolation can be formulated as follows:

$$\begin{cases} x_a = x_b + \mathbf{W}(y_o - \mathbf{H}x_b) \\ \mathbf{W} = \mathbf{B}\mathbf{H}^T(\mathbf{R} + \mathbf{H}\mathbf{B}\mathbf{H}^T)^{-1}, \end{cases} \quad (\text{D1})$$

where x_a is the desired analysis field, x_b is the background field, y_o represents observations at spaced points, \mathbf{H} is the observational operator that converts background fields into the “observed first guesses” and \mathbf{W} is the weight matrix that is calculated through the observational error covariance matrix \mathbf{R} and the background error covariance matrix \mathbf{B} . Assuming observational errors are spatially uncorrelated, the observational error covariance matrix \mathbf{R} is diagonal. Then, the element (i , j) of \mathbf{R} can be written as follows in Eq. (D2):

$$\mathbf{R}_{ij} = \sigma_o^2 \delta_{ij}, \quad (\text{D2})$$

where δ_{ij} is the Kronecker delta and σ_o is determined by the accuracies of the synthetic observations. The background error covariance matrix \mathbf{B} is estimated using an empirical formula:

$$\mathbf{B}_{ij} = \sigma_b^2 \exp\left[-(d_{ij}/L)^2\right], \quad (\text{D3})$$

where d_{ij} is the distance between two grids and σ_b is determined by the initial errors; L is the correlation length of matrix \mathbf{B} . Since the average radius of mesoscale eddies in the model adopted in the present study is 120 km and their related physical fields have a large gradient in the horizontal direction, the correlation length L associated with mesoscale eddies cannot be as large as that of large-scale circulation. Specifically, the length L here is experimentally adopted as 60 km.

REFERENCES

- Babiano, A., G. Boffetta, A. Provenzale, and A. Vulpiani, 1994: Chaotic advection in point vortex models and two-dimensional turbulence. *Phys. Fluids*, **6**, 2465–2474, <https://doi.org/10.1063/1.868194>.
- Barclay, A., P. E. Gill, and J. B. Rosen, 1997: SQP methods and their application to numerical optimal control. *Variational Calculus, Optimal Control and Applications, International*, W. H. Schmidt et al., Eds., Series of Numerical Mathematics, Vol. 124, Springer, 207–222.
- Birgin, E. G., J. M. Martínez, and M. Raydan, 2000: Nonmonotone spectral projected gradient methods on convex sets. *SIAM J. Optim.*, **10**, 1196–1211, <https://doi.org/10.1137/S1052623497330963>.
- Chelton, D., 2013: Mesoscale eddy effects. *Nat. Geosci.*, **6**, 594–595, <https://doi.org/10.1038/ngeo1906>.
- Chelton, D. B., M. G. Schlax, R. M. Samelson, and R. A. de Szoeke, 2007: Global observations of large oceanic eddies. *Geophys. Res. Lett.*, **34**, L15606, <https://doi.org/10.1029/2007GL030812>.
- , —, and —, 2011: Global observations of nonlinear mesoscale eddies. *Prog. Oceanogr.*, **91**, 167–216, <https://doi.org/10.1016/j.pocan.2011.01.002>.
- Cotton, P. D., and Y. Menard, 2006: Future requirements for satellite altimetry: Recommendations from the EC GAMBLE project. *15 Years of Progress in Radar Altimetry Symp.*, Venice, Italy, ESA, 13–18, <https://earth.esa.int/cgi-bin/confalt15yc7f7.html?abstract=946>.
- Dickey, T. D., F. Nencioli, V. S. Kuwahara, C. Leonard, W. Black, Y. M. Rii, R. R. Bidigare, and Q. Zhang, 2008: Physical and bio-optical observations of oceanic cyclones west of the island of Hawai'i. *Deep-Sea Res. II*, **55**, 1195–1217, <https://doi.org/10.1016/j.dsr2.2008.01.006>.
- Duan, W., and M. Mu, 2009: Conditional nonlinear optimal perturbation: Applications to stability, sensitivity, and predictability. *Sci. China*, **52D**, 883–906, <https://doi.org/10.1007/s11430-009-0090-3>.
- , and Z. H. Huo, 2016: An approach to generating mutually independent initial perturbations for ensemble forecasts: Orthogonal conditional nonlinear optimal perturbations. *J. Atmos. Sci.*, **73**, 997–1014, <https://doi.org/10.1175/JAS-D-15-0138.1>.
- , X. Li, and B. Tian, 2018: Towards optimal observational array for dealing with challenges of El Niño-Southern Oscillation predictions due to diversities of El Niño. *Climate Dyn.*, **51**, 3351–3368, <https://doi.org/10.1007/s00382-018-4082-x>.
- Faghmous, J. H., I. Frenger, Y. Yao, R. Warmka, A. Lindell, and V. Kumar, 2015: A daily global mesoscale ocean eddy dataset from satellite altimetry. *Sci. Data*, **2**, 150028, <https://doi.org/10.1038/sdata.2015.28>.

- Frenger, I., N. Gruber, R. Knutti, and M. Münnich, 2013: Imprint of Southern Ocean eddies on winds, clouds and rainfall. *Nat. Geosci.*, **6**, 608–612, <https://doi.org/10.1038/ngeo1863>.
- Fujii, Y., H. Tsujino, N. Usui, H. Nakano, and M. Kamachi, 2008: Application of singular vector analysis to the Kuroshio large meander. *J. Geophys. Res.*, **113**, C07026, <https://doi.org/10.1029/2007JC004476>.
- Gaube, P., D. J. McGillicuddy, D. B. Chelton, M. J. Behrenfeld, and P. G. Strutton, 2014: Regional variations in the influence of mesoscale eddies on near-surface chlorophyll. *J. Geophys. Res. Oceans*, **119**, 8195–8220, <https://doi.org/10.1002/2014JC010111>.
- Grooms, I., and A. J. Majda, 2014: Stochastic superparameterization in quasigeostrophic turbulence. *J. Comput. Phys.*, **271**, 78–98, <https://doi.org/10.1016/j.jcp.2013.09.020>.
- Hallberg, R., 2013: Using a resolution function to regulate parameterizations of oceanic mesoscale eddy effects. *Ocean Modell.*, **72**, 92–103, <https://doi.org/10.1016/j.ocemod.2013.08.007>.
- Kerswell, R. R., C. C. Pringle, and A. P. Willis, 2014: An optimization approach for analysing nonlinear stability with transition to turbulence in fluids as an exemplar. *Rep. Prog. Phys.*, **77**, 085901, <https://doi.org/10.1088/0034-4885/77/8/085901>.
- Lagerloef, G. S. E., and R. L. Bernstein, 1988: Empirical orthogonal function analysis of advanced very high resolution radiometer surface temperature patterns in Santa Barbara Channel. *J. Geophys. Res. Oceans*, **93**, 6863–6873, <https://doi.org/10.1029/JC093iC06p06863>.
- Li, Y., S. Peng, and D. Liu, 2014: Adaptive observation in the South China Sea using CNOP approach based on a 3-D ocean circulation model and its adjoint model. *J. Geophys. Res. Oceans*, **119**, 8973–8986, <https://doi.org/10.1002/2014JC010220>.
- Liao, G., X. Xu, C. Dong, H. Cao, and T. Wang, 2019: Three-dimensional baroclinic eddies in the ocean: Evolution, propagation, overall structures, and angular models. *J. Phys. Oceanogr.*, **49**, 2571–2599, <https://doi.org/10.1175/JPO-D-18-0237.1>.
- Liu, D. C., and J. Nocedal, 1989: On the limited memory BFGS method for large scale optimization. *Math. Program.*, **45**, 503–528, <https://doi.org/10.1007/BF01589116>.
- Michalakes, J., S. Chen, J. Dudhia, L. Hart, J. B. Klemp, J. Middlecoff, and W. Skamarock, 2001: Development of a next-generation regional weather research and forecast model. *Developments in Teracomputing: Proceedings of the Ninth ECMWF Workshop on the Use of High Performance Computing in Meteorology*, W. Zwiefelhofer and N. Kreitz, Eds., World Scientific, 269–276, https://doi.org/10.1142/9789812799685_0024.
- Morrow, R., and P.-Y. Le Traon, 2012: Recent advances in observing mesoscale ocean dynamics with satellite altimetry. *Adv. Space Res.*, **50**, 1062–1076, <https://doi.org/10.1016/j.asr.2011.09.033>.
- Mu, M., 2013: Methods, current status, and prospect of targeted observation. *Sci. China Earth Sci.*, **56**, 1997–2005, <https://doi.org/10.1007/s11430-013-4727-x>.
- , W. S. Duan, and B. Wang, 2003: Conditional nonlinear optimal perturbation and its applications. *Nonlinear Processes Geophys.*, **10**, 493–501, <https://doi.org/10.5194/npg-10-493-2003>.
- , F. Zhou, and H. Wang, 2009: A method for identifying the sensitive areas in targeted observations for tropical cyclone prediction: Conditional nonlinear optimal perturbation. *Mon. Wea. Rev.*, **137**, 1623–1639, <https://doi.org/10.1175/2008MWR2640.1>.
- , W. Duan, D. Chen, and W. Yu, 2015: Target observations for improving initialization of high-impact ocean-atmospheric environmental events forecasting. *Natl. Sci. Rev.*, **2**, 226–236, <https://doi.org/10.1093/nsr/nwv021>.
- , R. Feng, and W. Duan, 2017: Relationship between optimal precursors for Indian Ocean Dipole events and optimally growing initial errors in its prediction. *J. Geophys. Res. Oceans*, **122**, 1141–1153, <https://doi.org/10.1002/2016JC012527>.
- Pringle, C. C., and R. R. Kerswell, 2010: Using nonlinear transient growth to construct the minimal seed for shear flow turbulence. *Phys. Rev. Lett.*, **105**, 154502, <https://doi.org/10.1103/PhysRevLett.105.154502>.
- Qin, X., W. Duan, and M. Mu, 2013: Conditions under which CNOP sensitivity is valid for tropical cyclone adaptive observations. *Quart. J. Roy. Meteor. Soc.*, **139**, 1544–1554, <https://doi.org/10.1002/qj.2109>.
- Robinson, A. R., 1983: *Eddies in Marine Science*. Springer, 612 pp.
- Roemmich, D., and J. Gilson, 2001: Eddy transport of heat and thermocline waters in the North Pacific: A key to interannual/decadal climate variability? *J. Phys. Oceanogr.*, **31**, 675–687, [https://doi.org/10.1175/1520-0485\(2001\)031<0675:ETOHAT>2.0.CO;2](https://doi.org/10.1175/1520-0485(2001)031<0675:ETOHAT>2.0.CO;2).
- Shchepetkin, A. F., and J. C. McWilliams, 2005: The Regional Oceanic Modeling System (ROMS): A split-explicit, free-surface, topography-following-coordinate oceanic model. *Ocean Modell.*, **9**, 347–404, <https://doi.org/10.1016/j.ocemod.2004.08.002>.
- Snyder, C., 1996: Summary of an informal workshop on adaptive observations and FASTEX. *Bull. Amer. Meteor. Soc.*, **77**, 953–961, <https://doi.org/10.1175/1520-0477-77.5.953>.
- Tang, Q., S. P. S. Gulick, J. Sun, L. Sun, and Z. Jing, 2020: Submesoscale features and turbulent mixing of an oblique anticyclonic eddy in the Gulf of Alaska investigated by marine seismic survey data. *J. Geophys. Res. Oceans*, **125**, e2019JC015393, <https://doi.org/10.1029/2019JC015393>.
- Tsujino, H., N. Usui, and H. Nakano, 2006: Dynamics of Kuroshio path variations in a high-resolution general circulation model. *J. Geophys. Res.*, **111**, C11001, <https://doi.org/10.1029/2005JC003118>.
- Villas Bôas, A. B., O. T. Sato, A. Chaigneau, and G. P. Castelão, 2015: The signature of mesoscale eddies on the air-sea turbulent heat fluxes in the South Atlantic Ocean. *Geophys. Res. Lett.*, **42**, 1856–1862, <https://doi.org/10.1002/2015GL063105>.
- Wang, Q., M. Mu, and H. A. Dijkstra, 2013: The similarity between optimal precursor and optimally growing initial error in prediction of Kuroshio large meander and its application to targeted observation. *J. Geophys. Res. Oceans*, **118**, 869–884, <https://doi.org/10.1002/jgrc.20084>.
- Weiss, J. B., and I. Grooms, 2017: Assimilation of ocean sea-surface height observations of mesoscale eddies. *Chaos*, **27**, 126803, <https://doi.org/10.1063/1.4986088>.
- Wu, C.-C., J.-H. Chen, P.-H. Lin, and K.-H. Chou, 2007: Targeted observations of tropical cyclone movement based on the adjoint-derived sensitivity steering vector. *J. Atmos. Sci.*, **64**, 2611–2626, <https://doi.org/10.1175/JAS3974.1>.
- , and Coauthors, 2009: Intercomparison of targeted observation guidance for tropical cyclones in the northwestern Pacific. *Mon. Wea. Rev.*, **137**, 2471–2492, <https://doi.org/10.1175/2009MWR2762.1>.

- Yu, H., H. Wang, Z. Meng, M. Mu, X. Huang, and X. Zhang, 2017: A WRF-based tool for forecast sensitivity to initial perturbation: The conditional non-linear optimal perturbations versus the first singular vector method and comparison to MM5. *J. Atmos. Oceanic Technol.*, **34**, 187–206, <https://doi.org/10.1175/JTECH-D-15-0183.1>.
- Zhang, Y., X. Chen, and C. Dong, 2019: Anatomy of a cyclonic eddy in the kuroshio extension based on high-resolution observations. *Atmosphere*, **10**, 553, <https://doi.org/10.3390/atmos10090553>.
- Zhang, Z., Y. Zhang, W. Wang, and R. X. Huang, 2013: Universal structure of mesoscale eddies in the ocean. *Geophys. Res. Lett.*, **40**, 3677–3681, <https://doi.org/10.1002/grl.50736>.